Electrospun Au/CeO$_2$ nanofibers: A highly accessible, low pressure drop catalyst for preferential CO oxidation

Iván Moreno[a], Nuria Navascués[a], Silvia Irusta[a,b], Jesus Santamaria[a,b*]*

[a] Dept. Chemical Engineering, Nanoscience Institute of Aragon (INA), University of Zaragoza,

50018 Zaragoza, Spain

[b]Networking Research Center of Bioengineering, Biomaterials and Nanomedicine (CIBER-BBN).

Maria de Luna, 11. 50018 Zaragoza, Spain

sirusta@unizar.es, jesus.santamaria@unizar.es

Abstrac:

Au/CeO$_2$ catalysts shaped as nanofibers were obtained by supporting Au nanoparticles (ca. 3nm) on CeO$_2$ nanofibers of around 200 nm diameter. The CeO$_2$ support was prepared by calcining electrospun polymer nanocomposite fibers with a high Ce content, then gold nanoparticles were either synthesized *in situ* or deposited from a suspension. The prepared catalysts were used in the preferential oxidation of CO in a hydrogen-rich stream. The catalysts prepared by deposition of preformed gold nanoparticles were less stable, and underwent sintering due to a weaker nanoparticle-support interaction. In contrast, the catalysts with Au nanoparticles synthesized *in situ* were active (90% conversion and 46% selectivity) and stable. The fiber-shaped catalyst was able to give maximum reactant access at a much lower pressure drop compared to the catalyst in powder form.

1

INTRODUCTION

Hydrogen is widely considered as a highly promising, carbon-free energy carrier, especially for proton exchange membrane fuel cell (PEMFC) applications [1]. However, hydrogen must be obtained from other sources, and reforming of natural gas accounts for around 98% of hydrogen production worldwide [2]. Because the Pt anode of PEMFCs can be poisoned by CO the production of hydrogen fuel that is essentially CO-free (concentration around or below 10 ppm) is essential for PEMFC applications [3]. Among the various approaches for eliminating CO, preferential oxidation of CO by oxygen in excess H_2 (CO-PROX) is considered the most efficient solution [4]. The oxidation is rapid and responds quickly to changes in operating conditions, but it is essential to select catalysts and operating conditions that minimize the oxidation of hydrogen.

Selective oxidation can be achieved using different noble metal (Pt [5], Pd [6], Ru [7, 8], Rh [9], Ir[10, 11]), or transition metal-based (Cu [12, 13], Co [14], Mn[15]) catalysts but gold-based catalysts are among the most intensely investigated low temperature PROX catalysts [16]. The limited capacity of gold to chemisorb hydrogen is particularly advantageous to minimize the oxidation of H_2 into water. Gold supported on reducible oxides exhibits a higher activity for CO oxidation compared to the same catalyst on non-reducible oxides [17]. Among the reducible oxides, TiO_2 [18, 19], Fe_2O_3 [20], MnO_2 [21] and Co_3O_4 [22] have been reported as gold supports for the PROX reaction. CeO_2 is attractive as a support material, because of its ability to maintain a high dispersion of the active components and to change the oxidation state of the cation between +3 and +4 depending on the redox conditions [23]. Gold nanoparticles supported on pure ceria and various ceria-based mixed oxides were most frequently reported in the literature for the elimination of carbon monoxide from hydrogen rich streams [3, 24-28].

Conventional fixed-bed reactors (FBRs) randomly packed with catalysts particles are still widely used in industry for gas-solid processing. However, they present significant disadvantages that

may adversely affect the desired chemical reaction. Among these, high thermal resistance, high pressure drop, and low heat transfer coefficient have been cited [29]. In particular, FBRs face the central problem of balancing catalyst accessibility and reactor operability: as the catalyst particle becomes smaller, the external gas-solid interfacial area increases and the internal diffusion path decreases. The drawback is of course, the decrease of bed void fraction or porosity, ε, leading to a fast increase of pressure drop, as given by the Ergun equation:

$$\frac{\Delta P}{L} = 150 \frac{(1-\varepsilon)^2}{\varepsilon^3 d_p^2} \mu U_o + 1.75 \frac{(1-\varepsilon)^2 \rho_f}{\varepsilon^3 d_p} U_o^2$$

where $\Delta P/L$ is the pressure drop per unit length, d_p the particle diameter, U_o the superficial fluid velocity (volumetric flow rate per unit of cross sectional area) and ρ_f and μ the fluid density and viscosity respectively.

The strong dependence of pressure drop on bed porosity has been one of the main drivers for the development of structured catalytic beds together with an even flow pattern that narrows the residence time distribution [30]. However, structured packing is more expensive and complex to manufacture. The simplicity of a randomly packed catalyst would still be attractive, if the pressure drop problem could be alleviated. One of the possibilities to reduce pressure drop is the use of catalyst particles with a high aspect ratio, where random packing would spontaneously lead to higher bed porosity. From this point of view, catalysts with fiber morphology are highly desirable: the fiber diameter can be reduced to hundreds or even tens of nanometers, guaranteeing catalyst accessibility (negligible internal diffusion resistance) while maintaining a low pressure drop.

Electrospinning is a remarkably simple and powerful technique to generate continuous and thin fibers using a variety of different materials. Thanks to their small diameter and high porosity, electrospun materials have been used in biomedical applications, catalysis, nano-electronic devices, photovoltaics and nano-sensors [31]. For applications in catalysis, the one-

dimensional (1-D) polymer fibres that result from electrospinning can be used as templates for the synthesis of 1-D oxide catalysts. In this process polymer and inorganic precursor solutions are electrosprayed together to give a composite fiber containing the catalyst or catalyst precursors [32]. A posterior calcination process eliminates the polymer, yielding oxide fibers.

In this work, CeO_2 fibers were obtained by electrospinning and then gold nanoparticles were either synthesized *in situ* or deposited from a suspension on these fibers. The prepared solids were characterized by transmission electron microscopy (TEM), scanning electron microscopy (SEM), X-ray diffraction (XRD), X-ray photoelectron spectroscopy (XPS) and nitrogen adsorption. The Au/CeO_2 catalytic fibers were then used for the preferential oxidation of CO in a hydrogen-rich stream. The performance of the catalytic fibers matched that of powdered conventional catalyst at a much lower pressure drop.

EXPERIEMENTAL

Materials

Cerium nitrate hexahydrate ($Ce(NO_3)_3 \cdot 6H_2O$, Sigma Aldrich), poly(vinylpyrrolidone) (PVP Mw 1,300,000, Sigma Aldrich), gold (III) chloride hydrate ($HAuCl_4 \cdot H_2O$, 50% Au basis, Sigma Aldrich), ethanol (Sigma Aldrich), tetrakis(hydroxymethyl) phosphonium chloride solution (THPC, 80 wt% Aldrich), cerium(IV) oxide (CeO_2 nanopowder <25nm, Aldrich), sodium hydroxide (NaOH, 97%, Aldrich), hydrochloric acid (HCl, 37%, Aldrich), potassium chloride and distilled water reagents were used without further purification.

Methods

Catalysts preparation

The fibers were prepared in a 2.2.D-500 YFlow electrospinner, using solutions with different concentrations of Ce precursor and PVP. $Ce(NO_3)_3 \cdot 6H_2O$ (Ce1: 0.11g; Ce2: 0.22g; Ce3: 0.42g; Ce4: 0.18g; Ce5: 0.29g) was dissolved in an ethanol (10 ml)-water (2 ml) mixture under magnetic stirring for 15 minutes. Then, PVP (Ce1 and Ce2: 0.62g; Ce3: 0.75g; Ce4 and Ce5: 1g)

was added and the solution was kept under magnetic stirring overnight. The viscous Ce/PVP solution was loaded into a syringe connected with the inner part of the coaxial needle, and ethanol was used as shell liquid. The tip was placed at 25 cm of the collector plate. Pumps were set at 1ml/h for the inner solution and 0.2ml/h for the outer solution. Negative voltage of -2KV was connected to the collector plate and positive voltage was connected to the metallic needle. As-spun fibers were calcined at different temperatures (400ºC, 550ºC and 800ºC) for 6 hours with a heating slope of 0.5ºC/min. The calcined fibers were dispersed in a mixture of distilled water and ethanol in a ultrasonic bath during 15 minutes, then gold was incorporated to the ceria fiber by either of two different methods: i) impregnation with gold precursor to produce in-situ formation of Au nanoparticles, or ii) deposition of pre-synthesized Au nanoparticles.

For the first method an ethanol/water 10mM $HAuCl_4$ solution was added to the fibers dispersion, the pH was adjusted to 9 using a NH_3 solution and the mixture was put under magnetic stirring at 65ªC for 50 minutes. The amount of Au precursor was calculated to give a nominal gold load of 1.2%. In the second procedure, Au nanoparticles were separately synthesized by adding 0.5ml of 1M solution of NaOH to 45 ml of distilled water under magnetic stirring, then 12μl of THPC were added and the solution was kept under stirring for 5 minutes [33]. Finally, 2ml of 1wt.% $HAuCl_4$ solution were added and after 15 minutes reaction the product was refrigerated. These nanoparticles were deposited on CeO_2 by mixing 250 mg of CeO_2 fibers dispersed in distilled water with 25 ml of the gold NP suspension. The pH of the solution was adjusted to 2-3 with HCl 1M solution and kept under stirring for 24 hours. In both methods (i and ii) the fibers were finally thoroughly washed with water and centrifuged (20 min. at 4000 rpm) four times and then dried overnight at 100ºC. The absence of precursor residues and specifically of chloride and phosphorus-containing species, was confirmed by XPS analysis (Figure SI1). In this work, catalysts prepared by in-situ nucleation of Au nanoparticles on fibers calcined at 400, 550 and 800 ºC are denoted as Au/CeO_2(400), Au/CeO_2 (550) and

Au/CeO$_2$ (800) respectively. On the other hand, the catalyst obtained by deposition of pre-formed gold nanoparticles (method ii) is named AuNP/CeO$_2$ (550). For comparison, gold was also added to commercial ceria nanoparticles by method i), these samples are termed Au/CeO$_2$NP. Also for comparison, a sample with a larger particle size (between 1 and 2 mm) was prepared. To this end, the Au/CeO$_2$NP powder was pressed into a pellet using a laboratory press (10 ton), then crushed and sieved to the desired size.

Characterization

The solutions properties were characterized using a Fungilab Visco Basic Plus Viscometer and a ABB X400 conductivimeter. The prepared fibers were studied by scanning electron microscopy (SEM; FEI Inspect), and transmission electron microscopy (TEM FEI Tecnai F30 and probe aberration corrected FEI-Titan 60-300), to characterize fibers their size, morphology and gold nanoparticle distribution. The size distribution statistics were obtained by measuring at least 200 fibers or particles in different images. X-ray diffraction measurements of CeO$_2$ fiber were obtained using D-Max Rigaku 2500 X-ray diffractometer. The X-ray photoelectron analysis (XPS) was performed with an Axis Ultra DLD (Kratos Tech.). The spectra were excited by the monochromatized AlKα source (1486.6 e.V) run at 15 kV and 10 mA. The binding energies were referenced to the internal C 1s (284.9 eV) standard. The surface texture of samples was measured by nitrogen adsorption at 77K in a Micromeritics TriStar analyzer (Micromeritics, Norcross GA). Portions of 200 mg of every sample were outgassed at 26.7Pa and 623K for 6h. Surface area was determined using the BET equation, which was limited to the pressure range where the term Q(P$_0$-P) continuously increases with P/P$_0$. Z-potential analysis was carried out using a Brookhaven 90Plus Particle Size Analyzer using a suspension of the sample in 0.01M KCl solution and adjusting the pH of the solution.

Catalytic tests

The catalytic activity was measured in a packed bed reactor consisting of a quartz tube of 6 mm diameter loaded with 100 mg of catalyst. The WHSV was 1 ml min^{-1} mg^{-1}. The gas flow was 100 ml/min with the following composition: 1.3vol.% CO, 1.3vol.% O_2 and 97.4vol.% H_2. The stoichiometric ratio of oxygen atoms in the feed to CO was 2 (λ=2). The reaction temperature was measured with a thermocouple located in the center of the catalyst bed. The gas compositions at the inlet and outlet were measured by on-line gas chromatography (Varian MicroGC-4900, equipped with thermal conductivity detectors and two columns, CP740148 MS5A and CP740150 PPQ), allowing analysis of H_2, O_2, CO, CH_4, H_2O and CO_2, respectively. The mass balance was measured and was always in the range 98-102 at.%. CH_4 was not detected in any of the experiments carried out. The mass balance was measured and was always in the range 98-102 at.%. The CO conversion, the oxygen conversion and the selectivity of the PROX reaction were calculated according to the following equations:

$$CO\,conversion(\%) = \frac{F_{CO}^{Feed} - F_{CO}^{Outlet}}{F_{CO}^{Feed}} \times 100$$

$$O_2\,conversion(\%) = \frac{F_{O_2}^{Feed} - F_{O_2}^{Outlet}}{F_{O_2}^{Feed}} \times 100$$

$$Selectivity(\%) = 0.5 \times \frac{(F_{CO}^{Feed} - F_{CO}^{Outlet})}{(F_{O_2}^{Feed} - F_{O_2}^{Outlet})} \times 100$$

The conversion values were obtained after the reactor temperature was stable for at least 20 min and the values reported represent the average of 3 samples taken at the reactor exit.

The pressure drop along a randomly packed bed of the different catalytic materials was measured as a function of the flow rate. To facilitate the measurement, a standard Gems 3100B40 pressure transducer (0-40 kPa) was used in conjunction with a U-tube manometer containing mineral oil for a more accurate measurement in the low pressure range. To this end, 200 mg of CeO_2 fibers were loosely packed in a 6 mm internal diameter quartz tubular reactor. Then the same material was compacted by vibration and the pressure drop was measured again. Next, the fibers were unloaded and ground to a particle size between 1 and

20 microns. Then the powder was repacked, first loosely and then in a compact way and the pressure drop was measured again as a function of the flow rate.

RESULTS AND DISCUSSION

CeO$_2$ fibers characterization

Solutions with different PVP concentration and weight ratios of cerium to polymer were prepared and tested under electrospinning conditions (Table 1). The morphology of the samples obtained was very different, depending on the solution used. Solutions with low polymer concentration (5.8 and 7.3 wt.%) and high Ce(NO$_3$)$_3$ content produced unstable Taylor cones and it was not possible to electrospin them. The amount of PVP was found to be an important cause of the change in viscosity of the sol and, as expected, the viscosity of the sol increased with increasing PVP content [34]. A minimum viscosity value is necessary to overcome the surface tension effects and produce fibers [35]. On the other hand, it is known that a high solution conductivity results in a high degree of stretching and important viscoelastic forces in the electrospinning jets [36]. The decrease in the Ce precursor/polymer ratio from 0.114 to 0.057 reduces the solution conductivity [37] while keeping similar value of viscosity. This value of viscosity enables electrospinning but the product consist of beaded fibers as shown in Figure 1 a. Increasing the PVP concentration to 9 wt.% at the same Ce(NO$_3$)$_3$ / PVP ratio increases the viscosity without important changes in conductivity and as a consequence bead-free fibers (sample Ce4) can be obtained. Since a further increase of the cerium precursor concentration (sample Ce5) also produces bead-free fibers, in order to increase the production of inorganic fibers the solution parameters of sample Ce5 were used. This produced uniform smooth fibers with a diameter of 647± 80 nm (Figure 1 b and c).

Table 1: Polymer/precursor solution properties

Sample	PVP concentration (wt%)	Ce(NO$_3$)$_3$ / PVP Mass ratio	Viscosity	Conductivity	Results
Ce1	7.3	0.180	160.2 cP	752 µS/cm	-
Ce 2	5.8	0.114	78.5 cP	727 µS/cm	-
Ce 3	5.8	0.057	75.5 cP	402 µS/cm	Beads
Ce 4	9.0	0.058	299.6 cP	442 µS/cm	Fibers
Ce 5	9.0	0.187	391.0 cP	522 µS/cm	Fibers
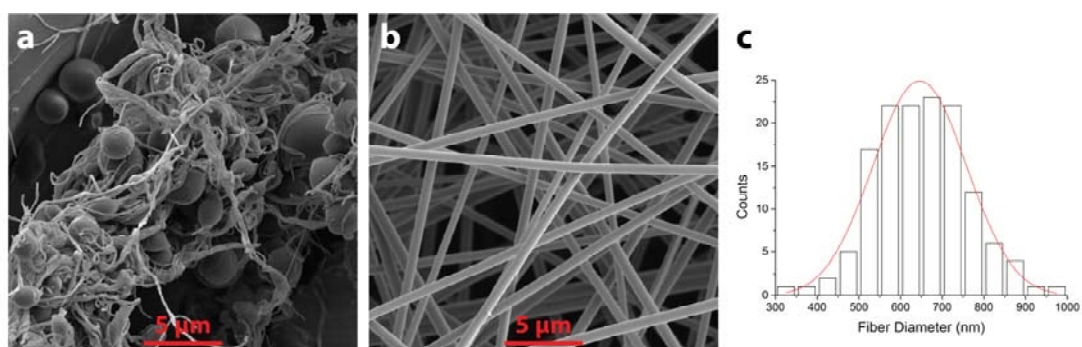
Figure 1: SEM images of as spun a) Ce1 fibers; b) Ce5 fibers; c) size diameter distribution for Ce5.
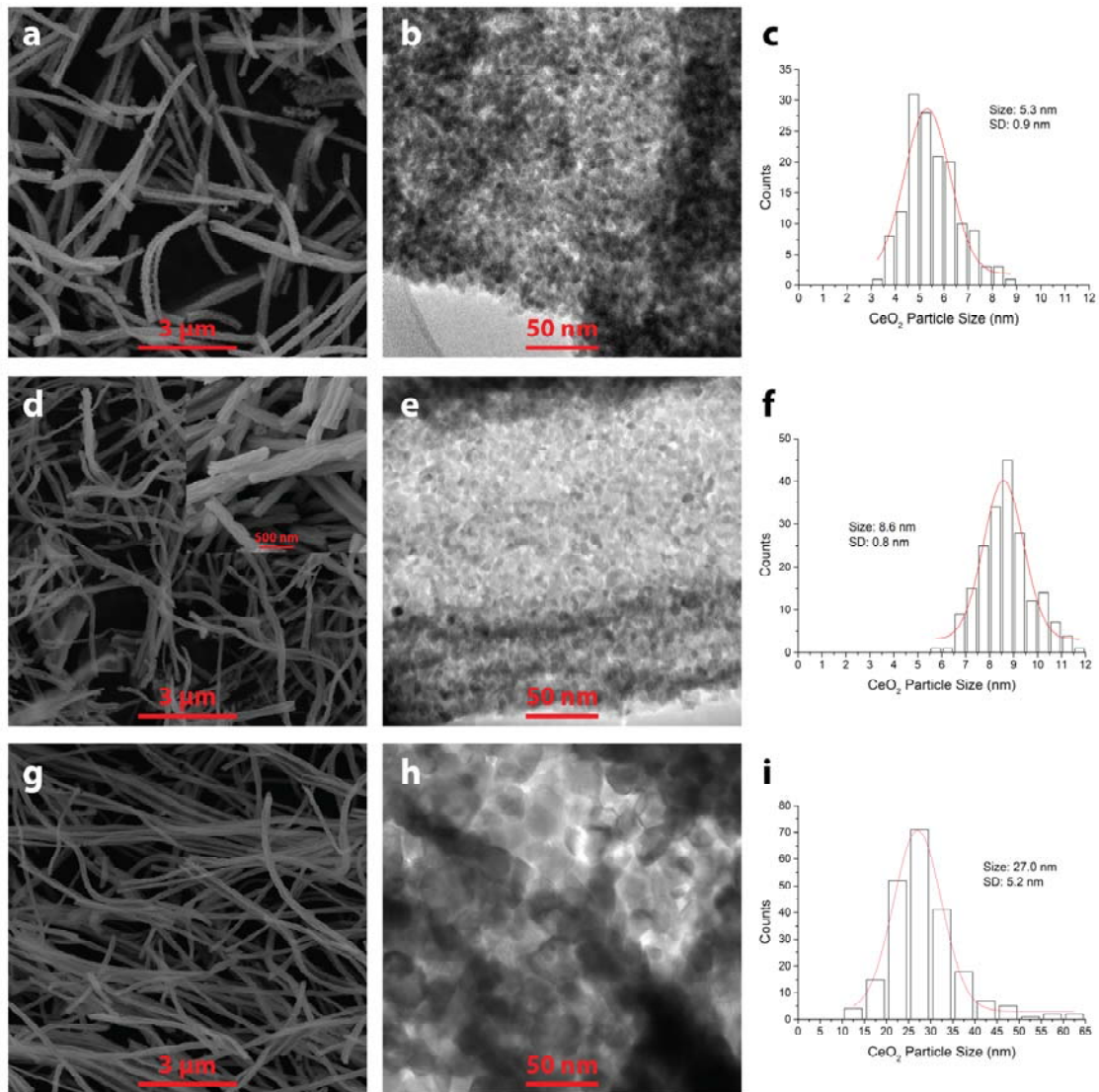
Figure 2: SEM images of CeO$_2$ fibers calcined at a) 400ºC, d) 550 ºC and g) 800 ºC, TEM images of fibers calcined at b) 400ºC, e) 550 ºC and h) 800 ºC; size distribution of the primary CeO$_2$ nanoparticles c) 400ºC, f) 550 ºC and i) 800 ºC. Magnification of fibers is shown in the inset of d).

Calcination at 400, 550 or 800 ºC was used to produce inorganic fibers from the polymer composite fibers. SEM images of calcined samples are shown in Figure 2. It can be observed that the fiber diameter undergoes a strong contraction after calcination due to the removal of PVP and decomposition of oxide precursor and this contraction increases with calcination

temperature (Table 2). Thus, after calcination diameters (over 200 fibers measured), decreased from around 650 nm to less than 250 nm. The decrease in the diameter of the calcined fibers from 236 (calcination at 400 ºC) to 158 nm (800 ºC) can be attributed to increased sintering since TGA analysis shows no significant weight loss in the calcined fibers even for the lowest calcination temperature (Figure SI2). Even though the length of the fibers was very difficult to measure due to their partial entanglement and to their broad size distribution due to their irregular breaking as a result of the calcination, in most cases their aspect ratio appeared to be in the 10-100 range. Most of the grains forming CeO_2 fibers are homogeneous with an average particle size calculated from the TEM images of 5.31, 8.58 and 27.0 nm for 400, 550 and 800 ºC calcination temperature respectively. As expected, sintering processes accelerate with temperatures above a certain threshold and the growth of the primary ceria nanoparticles that conform the fibers is enhanced at higher calcination temperatures [38]. A closer analysis of the fibers calcined at intermediate temperatures (inset in Figure 2) shows that the fibers of 194 nm diameter are formed by thinner fibers of around 40 nm diameter.

XRD patterns of ceria fibers calcined at different temperatures are shown in Fig. 3. The diffraction peaks correspond to the (111), (200), (220) and (311) planes, which can be indexed to pure cubic fluorite structure for cerium oxide (fcc, JCPDS34-0394)[39]. Broad peaks observed for samples calcined at 400 and 550 ºC indicate smaller crystal size, compared to the sharper peaks of the sample calcined at 800 ºC are sharper, attributed to the increase in crystal size as a result of the sintering process, in agreement with TEM results. Crystallite sizes calculated with the Scherrer equation correspond well to the particle size measured from TEM images (Table 2). The surface areas of samples calcined at different temperatures are also given in Table 2, and they confirm the strong sintering process at higher calcination temperatures: roughly three quarters of the surface area is lost when the calcination temperature increases from 400 to 800 ºC. The measured BET areas are of the same order of

magnitude as the areas calculated for dense spheres using the average mean diameter obtained from TEM images. This indicates that the fibers are composed by an agglomeration of dense primary CeO_2 nanoparticles, with negligible internal porosity.
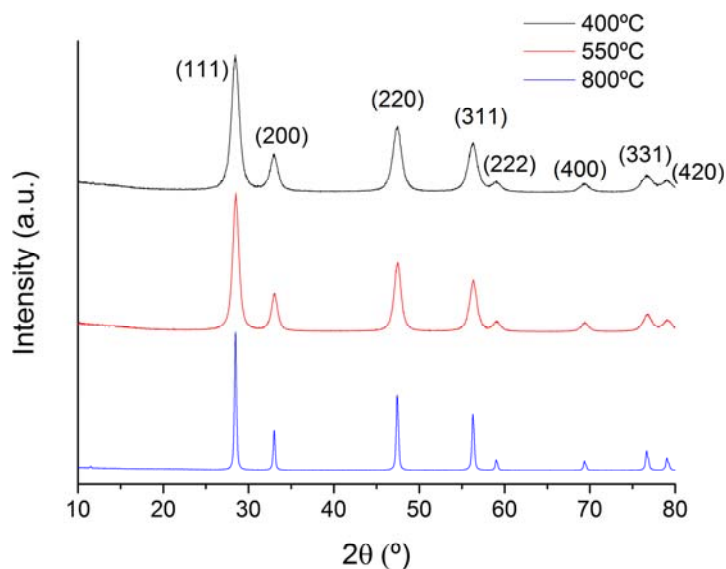

Figure 3: X-ray diffraction pattern of fibers calcined at different temperatures.

Table 2: Characterization results of CeO_2 fibers and commercial nanoparticles

Material/Calcination temperature	Fiber diameter (nm)	Particle size[a] (nm)	Crystallite size (nm)	S_A (BET) (m^2/g)	$S_A{}^b$ (m^2/g)
Fiber/400 ºC	236 ± 41	5.3 ± 0.9	7.2 ± 0.2	-	155
Fiber/550 ºC	194 ± 38	8.6 ± 0.8	9.4± 0.5	94	97
Fiber/800 ºC	158 ± 33	27.0 ± 0.2	29.4± 0.5	13	28

Commercial nanoparticles/uncalcined	N/A	12.3±3.8	-	45	33

[a] From size distribution obtained from TEM images

[b] BET nominal area calculated for spheres with a mean diameter equal to that obtained from TEM images for the primary ceria nanoparticles.

Catalysts characterization

In order to optimize conditions for the attachment of pre-synthesized nanoparticles to the fibers, the surface charge of both materials was studied. In the ζ−potential versus pH plot (Figure SI3), the surface charge of ceria fibers varied between +10 and -30 mV, with an isoelectric point at pH=4, whereas for Au nanoparticles the surface charge was always below -19 mV. According to these results the pH of the impregnating solution was adjusted between 2 and 3 to obtain charges of opposite sign between CeO_2 and Au, using HCl acid.

Analysis by HRTEM was carried out on all the Au/CeO_2 solids to determine the size and distribution of gold nanoparticles on ceria fibers (Figure 4). The distribution of particle sizes is shown in Figure 4. On supports calcined at 550 and 800 ºC the size of in-situ formed gold nanoparticles is around 3nm (2.7 and 3.4 nm respectively, Table 3). Gold nanoparticles on $Au/CeO_2(800)$ were analyzed using an ultra-high resolution TEM (Figure 5). The calculate d-spacing corresponds to that of metallic gold. On the other hand, in ceria fibers calcined at low temperature it was not possible to obtain the size distribution of AuNP because the identification of smaller gold nanoparticles from ceria nanoparticles (size ≈5 nm) is hardly noticeable due to poor contrast between the Au and cerium [40]. Previous literature reports confirm the difficult detection of gold nanoparticles on CeO_2 using TEM when the metal dispersion is very high [41].

When preformed Au nanoparticles were deposited on fibers calcined at 550ºC from a nanoparticle suspension (method ii) their size increased from 2.0 to 4.1 nm after deposition, as can be seen by comparing the particle size distribution in the suspension and on the support (Figure 6). The different particle size distribution gives some clues on the interaction of gold and ceria: when the Au NPs are produced *in situ* by impregnation with gold precursor the anchoring of gold is favored, since it is known that $Au^{\delta+}$ species strongly interact with ceria nanoparticles [42]. The evolution of the newly formed Au clusters is intimately associated with their bonding strength with surface oxygen-deficient ceria: their strong bonding stabilizes metal nanoparticles against sintering [43]. On the other hand, pre-synthesized particles deposited onto fibers would have weaker interaction with the support which facilitates agglomeration during the deposition process. Any remaining THPC on the surface of the gold nanoparticles would further contribute to this lower nanoparticle-support interaction.

Figure 4: TEM micrograph of Au nanoparticles formed on ceria fibers calcined at a) 400ºC, b) 550ºC and d) 800ºC; Au particle size distributions on support calcined at c) 550ºC and e) 800ºC.
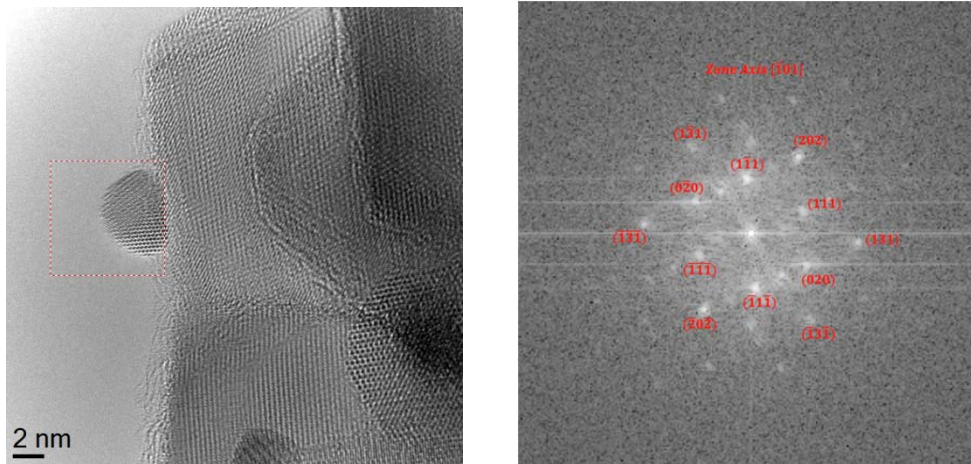
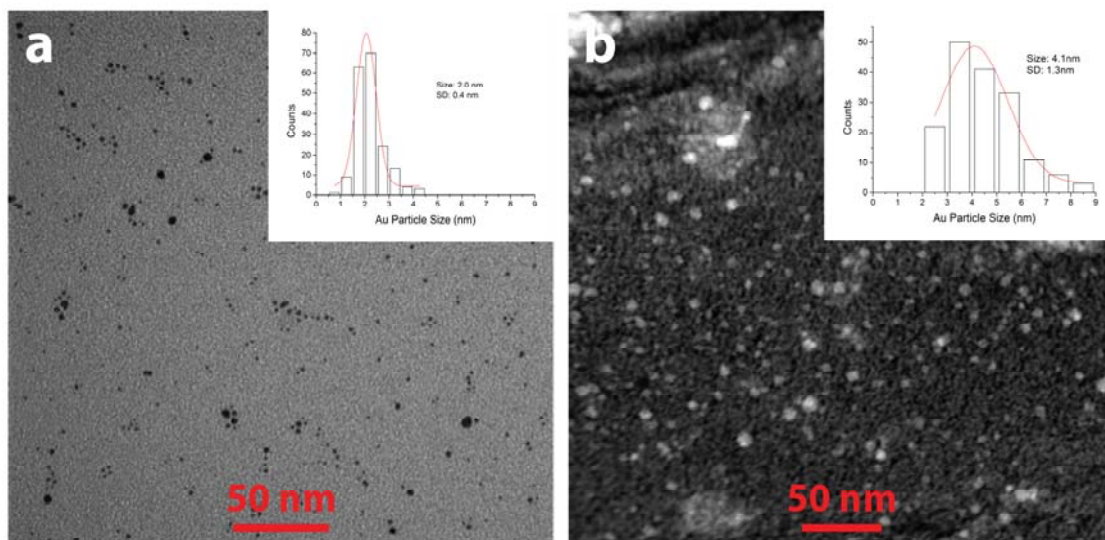Figure 5: TEM image of Au/CeO$_2$(800) and Fourier mask filtering of the FFT pattern.

Figure6 : TEM image of synthesized gold nanoparticles a) in suspension and b) deposited on

ceria fibers previously calcined at 550ºC. Insets show the particle size distribution.

Table 3: Au/Ce catalysts characterization

Catalyst	Au load (wt.%)	Au NP size (nm)	X_{Max}	S^1	T^1 (ºC)	$ATOF^2$ (s^{-1})
Au/CeO$_2$(400)	1.04	-	75.5%	37.9%	125	
Au/CeO$_2$(550)	1.00	2.7	88.2%	45.8%	75	0.39
Au/CeO$_2$(800)	1.57	3.4	90.3%	47.1%	100	0.32
AuNP/CeO$_2$ (550)	1.32	4.1	27.2%	20.1%	150	0.13
Au/CeO$_2$NP (550)	1.08	2.7	83.8%	41.7%	75	0.31

[1] Selectivity and temperature at which the maximum conversion was obtained

[2] The ATOF values are nominal TOF values calculated using the average particle size estimated from TEM observations. Average (ATOF) values were used because, due to the high conversion values obtained, the TOF values are not homogeneous throughout the catalytic bed.

The surface composition the prepared solids was characterized by XPS. The Ce 3d core level spectrum of all the catalysts is very similar in spite of the different calcination temperatures (Figure SI4) and shows the predominance of the +4 state, indicated by the main $3d_{5/2}$ component at 882.0 eV (v) and also by a prominent peak at approximately 916.5 eV (u´´) [44]. It must be however noticed that some Ce(III), is present in the catalyst, as indicated by the shoulders at about 880.5 and 885.5 eV related to peaks v_0 and v´, [45]. It is known that the high content of Ce^{3+} ions and oxygen vacancies, has promotional effect for CO oxidation of Au/CeO$_2$ catalysts [46].

Au 4f level was analyzed in fresh and used samples with the results shown in Table 4 and Figures SI5. For fresh catalysts two doublets for Au 4f, $4f_{7/2}$ and $4f_{5/2}$, due to spin orbit splitting were observed. Peaks at lower binding energy were assigned to metallic gold [41] while peaks at higher binding energy (84.4-84.8 eV) could be related to oxidized gold species [46]. The concentration of metallic gold species was higher for the solids calcined at 550 and 800 ºC while for Au/CeO_2 (400) it only reached 57%. It was reported that CeO_2 could inhibit gold reduction in air through the dynamic effect of surface defects, stabilizing the cationic Au by a strong chemical interaction [47]. Even though it was not possible to detect differences in the Ce^{3+} concentration for the supports from Ce 3d spectra in this case, it is expected that for the support calcined at lower temperature the number of defects is larger and this would explain the higher oxidation state of gold in $Au/CeO_2(400)$ [48]. Another interesting feature is the Au/Ce atomic ratio, that for almost the same gold loading is much lower for the solid calcined at 400 ºC. This can be explained as a consequence of the progressive sintering of the CeO_2 support that takes place at higher calcination temperatures (BET surface areas decrease from 125 m^2/g for the sample calcined at 400 ºC to 28 m^2/g for the 800ºC sample). Thus, for the same overall Au/Ce ratio and a similar size of the Au nanoparticles, the surface Au/Ce ratio is expected to increase with calcination temperature, as reflected in the XPS results. After reaction the metallic gold concentration increased for the three solids, reaching 100% in the catalysts supported on solids calcined at higher temperatures (550 and 800ºC). This is important because the presence of Au^0 is required to obtain an active Au/CeO_2 catalyst [46, 47]. The fact that around 1 in 5 gold atoms is still oxidized in the sample calcined at lower temperature $Au/CeO_2(400)$ could be related to the already mentioned interaction between gold nanoparticles and ceria.

Table 4: Au 4 f$_{7/2}$ core level results

Catalyst	Fresh			Used	
	Au^0	Au$^{\delta+}$	Au/Ce	Au^0	Au$^{\delta+}$
Au/CeO$_2$ (400)	83.7	84.4	0.0068	83.8	84.4
	57%	43%		73%	17%
Au/CeO$_2$ (550)	83.9	84.8	0.0370	83.7	-
	94%	6%		100%	
Au/CeO$_2$(800)	83.5	84.5	0.0489	83.8	-
	80%	20%		100%	

Catalytic tests

Mass transport and heat transfer calculations were carried out for the highest rates and according to the Weisz-Prater criterion (C$_{WP}$<1) there were no internal limitations. It was also found that no interphase and intraparticle heat transfer or mass transport limitations exist in the system according to Mears criterion (See supplementary information) [49].

Figure 7 illustrates the catalytic activity of solids prepared with gold nanoparticles formed *in situ* after impregnation with gold precursor. The results are shown for fibers calcined at different temperatures in terms of CO conversion and PROX selectivity. With all samples, the characteristic maximum in the CO conversion curve with temperature was observed. Since oxygen is the limiting reactant and there are two competing reactions (CO and hydrogen oxidation), a decrease in CO conversion with increasing temperature is eventually observed due to the acceleration of the undesired hydrogen oxidation [50]. The lowest conversion was obtained with catalysts prepared on supports calcined at 400ºC, reaching less than 80 % CO conversion (Table 3) at any temperature, with the maximum conversion at 125 ºC. On the

other hand, with Au/CeO$_2$(550) and Au/CeO$_2$(800) the conversions were considerably higher (around 90%), driven by a higher selectivity. The higher proportion of metallic gold in the catalysts calcined at higher temperatures would explain the superior performance of the catalysts prepared at 550 and 800 ºC, in spite of their lower surface areas.
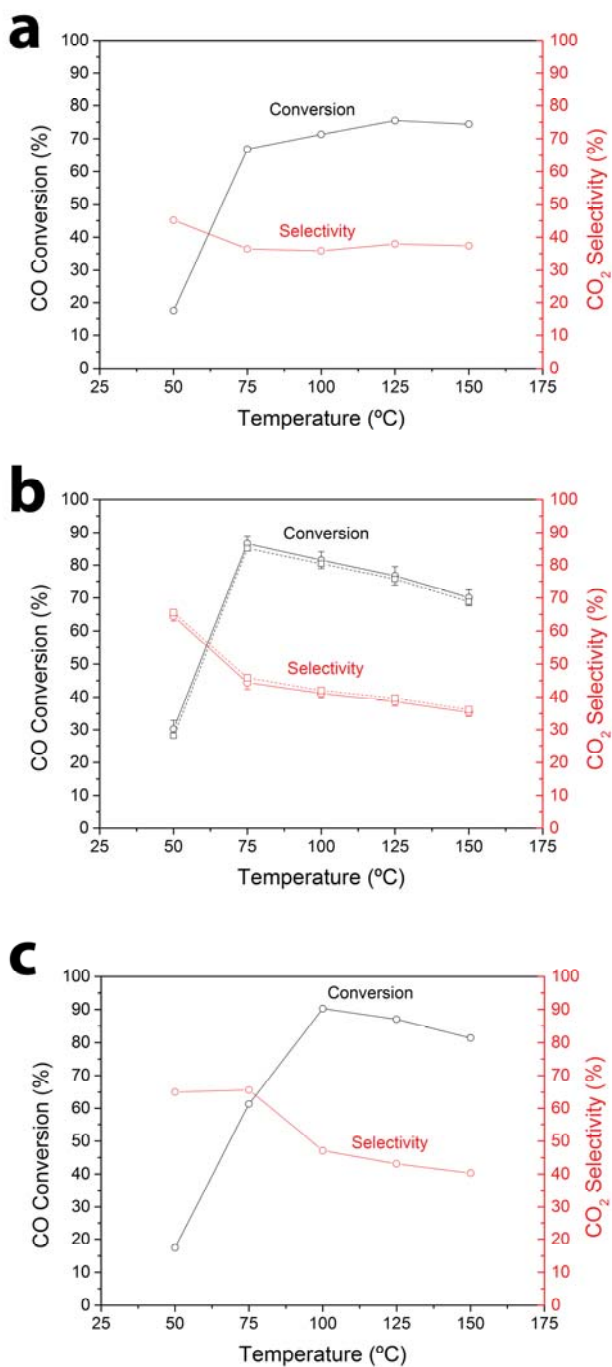

Figure 7: Catalytic behavior of catalysts a) Au/CeO$_2$(400), b) Au/CeO$_2$(550), dotted line is for decreasing temperature, and c) Au/CeO$_2$(800).
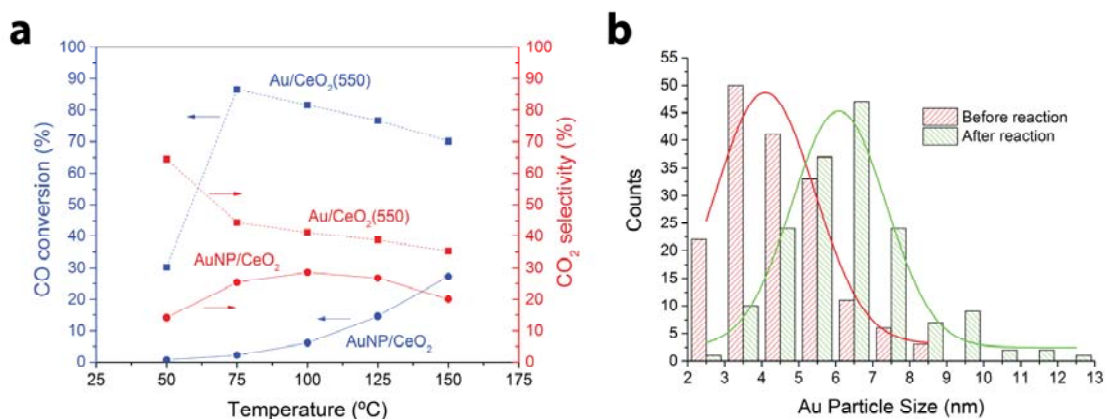
Figure 8: a) CO conversion and selectivity over catalysts obtained either *in situ,* by impregnation with Au precursor (Au/CeO$_2$) or from pre-synthesized Au nanoparticles (AuNP/CeO$_2$), b) Au particle size distribution before and after reaction for AuNP/CeO$_2$.

The catalytic behavior of solids prepared by different methods is shown in Figure 8. Since the support is the same for both catalysts, the size of gold nanoparticles and the interaction with the support would be responsible for the different behavior observed and in particular for the lower activity of the AuNP/CeO$_2$ catalyst. It was reported that CO oxidation reaction readily occurred at perimeter sites between Au and oxide [51], stressing the importance of the interaction between Au nanoparticles and CeO$_2$. From this point of view, the *in situ* synthesis of gold nanoparticles would be preferred, as a method that favors such interaction, in contrast with the deposition of preformed nanoparticles, where interaction would be weaker. Since it has been reported that the surface oxygen vacancies on ceria stabilize metal nanoparticles against sintering through strong chemical bonding [43], the degree of sintering could be used as an indirect measurement of the interaction between the CeO$_2$ support and the Au clusters.

While the concept of using preformed Au nanoparticles is attractive because it increases the degree of control over the initial particle size, this method is not adequate, due to the weak

interaction of the metal nanoparticles with the ceria support. Thus, as already shown, the size of metal nanoparticles quickly doubles upon deposition from the initial 2.0 to 4.1 nm. As a consequence of this weak metal-support interaction the AuNP/CeO$_2$ catalyst displays not only a lower initial activity, but also a significant sintering under the reaction conditions used, with a strong increase of the mean particle size from 4.1 to 6.1 nm, after only 5 hours of reaction (Figure 8b).

This is in contrast with the results obtained for the catalyst prepared in situ. In this case, the increase in the mean particle size for the Au/CeO$_2$(550) catalyst was almost negligible (figure 9b), which is in agreement with the stable performance observed during 48 h of operation (Figure 9a) reflecting the stronger interaction between the gold and ceria nanoparticles in the catalyst prepared *in situ*, which prevents deactivation of the catalyst by sintering [52].
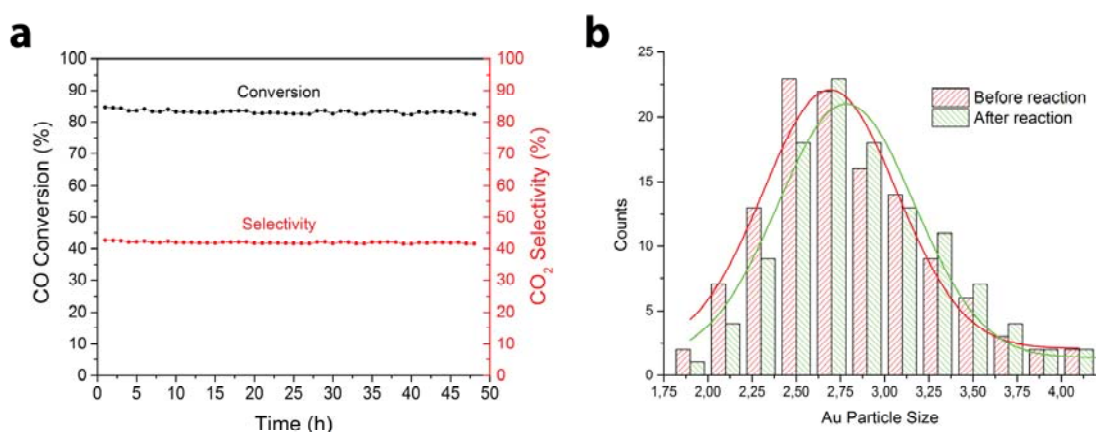

Figure 9: a) Long term stability test for Au/CeO$_2$(550) at 75 ºC, b) particle size distribution after 48 h under reaction

For the Au/CeO$_2$(550) catalysts a dispersion of 41.4 % was estimated from TEM images following the procedure described by Collins et al. [53] and the average turnover frequency (ATOF) value calculated from this dispersion was 0.39 s^{-1}. In order to compare the catalytic behavior of this solid with reported values, recent literature reports using Au/CeO$_2$ catalysts

under similar values of WHSV and the same λ were selected (Table 5). Since not all the manuscripts report the Au dispersion values, the nominal TOF values reported on the table were calculated assuming 100 % dispersion.
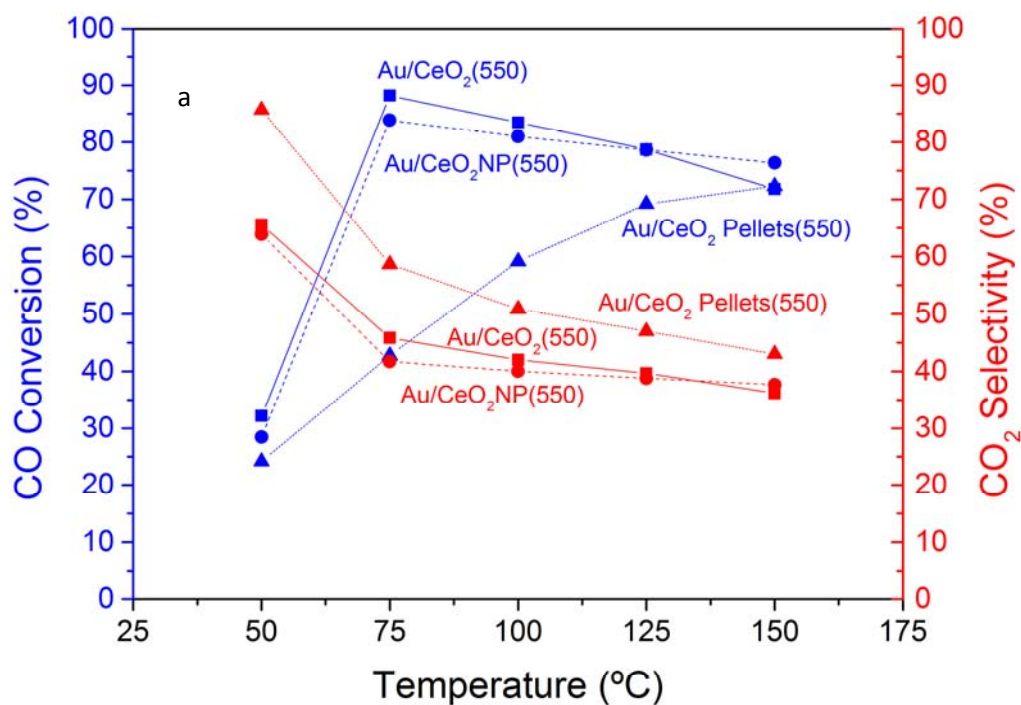
Table 5: Comparison of the catalytic behavior of different Au/CeO_2 catalysts for the PROX reaction at $\lambda=2$.

Au load	Space velocity	TOF[1]	T	Reference
(wt%)	$(ml.mg^{-1}.min^{-1})$	mol $CO.mol Au^{-1}.s^{-1}$	(ºC)	
1.00	1.0	0.16	75	This work
0.85	0.5	0.16	75	[41]
4.30	1.6	0.05	40	[54]
1.00	1.0	0.28	90	[55]
0.65	0.5	0.11	40	[56]
1.40	1.0	0.08	100	[57]

[1] These are nominal value, calculated assuming a gold dispersion of 100% for all samples.

In Figure 10a the performance of Au nanoparticles supported on fiber-, pellet- and powder-shaped catalyst are compared. It can be seen that the performance of the powder catalyst is close to that of the nanofibers, both in terms of conversion and selectivity. This was expected since the fibers are being compared to a powdered catalyst formed by nanoparticles in agglomerates with open structure and an average size around 26 microns. At this low particle size, and at the low temperatures of the PROX reaction, internal diffusion resistances are negligible. However, spherical particles of that size cannot be used in large packed bed

reactors due to the high pressure drop involved. As an example, in figure 10b the pressure

drop is compared for fiber and powder catalysts (see experimental section for details), and it

can be seen that the pressure drop is roughly doubled when the same mass of catalyst is used

in powdered form, both in the loosely packed and in the compacted catalyst beds. This is

remarkable because the average diameter of the fiber shaped catalyst is only around 200 nm,

i.e., at a much lower pressure drop it provides diffusion lengths that are two orders of

magnitude smaller, even when compared to the powdered catalyst used in this example. The

pressure drop for the particles (1 to 2 mm) was also negligible, as expected, given the size of

the packed bed used. However, pelletizing the nanoparticles even to this small size has an

immediate effect on conversion: Figure 10a shows that the conversion achieved was much

lower than for powder and fiber-shaped solids due to the lower accesibility of the catalytic
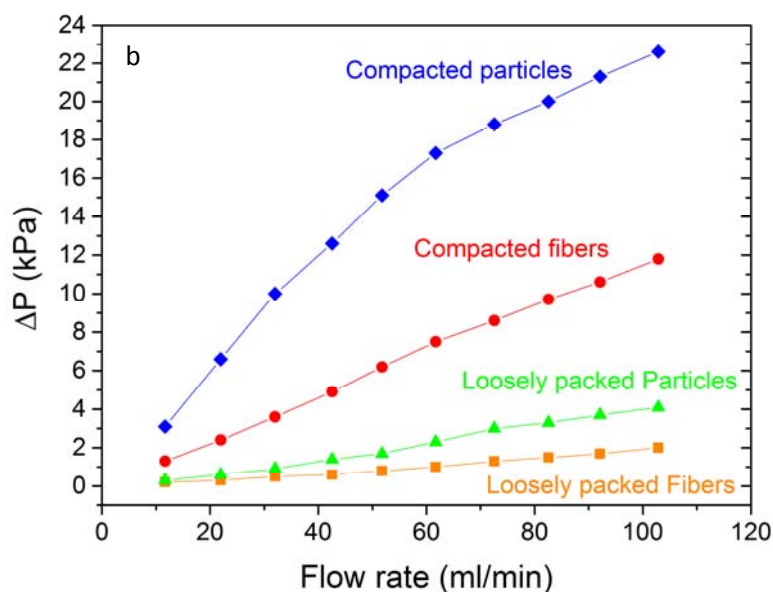
sites as particle size increased.

Figure 10: a) Comparison of the catalytic behavior of gold nanoparticles onto ceria nanoparticles in powder form (Au/CeO$_2$NP), the powder in form of pellets and the Au/CeO$_2$ catalyst shaped as fibers. Both supports were calcined at 550 ºC. b) Pressure drop as a function of flow rate for randomly packed beds of powder and fiber-shaped catalysts

CONCLUSIONS

Electrospun polymer nanofibers with a high Ce content can be used as suitable precursors to prepare Au/CeO$_2$ catalysts that are active and selective for the preferential oxidation of CO. The best results were obtained on catalysts with nanoparticles formed *in situ* on supports calcined at 550 and 800 ºC, due to a high proportion of metallic gold, a good dispersion and a low non-selective contribution of the CeO$_2$ support. Catalyst prepared with preformed Au NP showed deactivation by sintering as a consequence of the weak interaction between the CeO$_2$ support and the Au clusters. In contrast, the Au/CeO$_2$(550) catalyst showed a stable performance, due to a stronger anchoring of the Au nanoparticles produced *in situ*. The high aspect ratio of the fiber-shaped catalysts gives rise to randomly packed beds with a much higher porosity. As a consequence, fibers with a diameter around 200 nm (and therefore with

25

diffusion lengths that are orders of magnitude smaller than the 20-30 micron particles) present

half of the pressure drop than comparable powdered catalysts.

Acknowledgments

References

[1] A. Luengnaruemitchai, S. Chawla, R. Wanchanthuek, The catalytic performance of Au/La-CeOx catalyst for PROX reaction in H2 rich stream, International Journal of Hydrogen Energy, 39 (2014) 16953-16963.
[2] M.N. Uddin, W.M.A.W. Daud, Technological Diversity and Economics: Coupling Effects on Hydrogen Production from Biomass, Energy & Fuels, 28 (2014) 4300-4320.
[3] P. Lakshmanan, J.E. Park, E.D. Park, Recent Advances in Preferential Oxidation of CO in H-2 Over Gold Catalysts, Catalysis Surveys from Asia, 18 (2014) 75-88.
[4] E.D. Park, D. Lee, H.C. Lee, Recent progress in selective CO removal in a H2-rich stream, Catalysis Today, 139 (2009) 280-290.
[5] K.Y. Koo, U.H. Jung, W.L. Yoon, A highly dispersed Pt/γ-Al2O3 catalyst prepared via deposition–precipitation method for preferential CO oxidation, International Journal of Hydrogen Energy, 39 (2014) 5696-5703.
[6] H. Zhang, M. Jin, H. Liu, J. Wang, M.J. Kim, D. Yang, Z. Xie, J. Liu, Y. Xia, Facile Synthesis of Pd-Pt Alloy Nanocages and Their Enhanced Performance for Preferential Oxidation of CO in Excess Hydrogen, Acs Nano, 5 (2011) 8212-8222.
[7] T. Niu, L.H. Zhang, Y. Liu, Highly dispersed Ru on K-doped meso-macroporous SiO2 for the preferential oxidation of CO in H-2-rich gases, International Journal of Hydrogen Energy, 39 (2014) 13800-13807.
[8] X. Chen, J.J. Delgado, J.M. Gatica, S. Zerrad, J.M. Cies, S. Bernal, Preferential oxidation of CO in the presence of excess of hydrogen on Ru/Al2O3 catalyst: Promoting effect of ceria-terbia mixed oxide, Journal of Catalysis, 299 (2013) 272-283.
[9] T. Niu, C.X. Wang, L.H. Zhang, Y. Liu, Potassium promoted Ru/meso-macroporous SiO2 catalyst for the preferential oxidation of CO in H-2-rich gases, International Journal of Hydrogen Energy, 38 (2013) 7801-7810.
[10] L. Piccolo, S. Nassreddine, F. Morfin, Surface study of the hydrogen-free or preferential oxidation of CO: Iridium vs. platinum, Catalysis Today, 189 (2012) 42-48.
[11] J. Lin, B. Qiao, L. Li, H. Guan, C. Ruan, A. Wang, W. Zhang, X. Wang, T. Zhang, Remarkable effects of hydroxyl species on low-temperature CO (preferential) oxidation over Ir/Fe(OH)(x) catalyst, Journal of Catalysis, 319 (2014) 142-149.
[12] M. Monte, D. Gamarra, A.L. Camara, S.B. Rasmussen, N. Gyorffy, Z. Schay, A. Martinez-Arias, J.C. Conesa, Preferential oxidation of CO in excess H-2 over CuO/CeO2 catalysts:

Performance as a function of the copper coverage and exposed face present in the CeO2 support, Catalysis Today, 229 (2014) 104-113.

[13] R. Zhang, J.T. Miller, C.D. Baertsch, Identifying the active redox oxygen sites in a mixed Cu and Ce oxide catalyst by in situ X-ray absorption spectroscopy and anaerobic reactions with CO in concentrated H-2, Journal of Catalysis, 294 (2012) 69-78.

[14] Z. Zhao, J. Lin, G. Wang, T. Muhammad, Novel Co-Mn-O Nanosheet Catalyst for CO Preferential Oxidation Toward Hydrogen Purification, Aiche Journal, 61 (2015) 239-252.

[15] Z. Zhao, T. Bao, Y. Li, X. Min, D. Zhao, T. Muhammad, The supported CeO2/Co3O4-MnO2/CeO2 catalyst on activated carbon prepared by a successive-loading approach with superior catalytic activity and selectivity for CO preferential oxidation in H-2-rich stream, Catalysis Communications, 48 (2014) 24-28.

[16] M. Kipnis, Gold in CO oxidation and PROX: The role of reaction exothermicity and nanometer-scale particle size, Applied Catalysis B: Environmental, 152–153 (2014) 38-45.

[17] K. Yang, Y. Li, K. Huang, X. Chen, X. Fu, W. Dai, Promoted effect of PANI on the preferential oxidation of CO in the presence of H2 over Au/TiO2 under visible light irradiation, International Journal of Hydrogen Energy, 39 (2014) 18312-18325.

[18] D. Widmann, E. Hocking, R.J. Behm, On the origin of the selectivity in the preferential CO oxidation on Au/TiO2 - Nature of the active oxygen species for H-2 oxidation, Journal of Catalysis, 317 (2014) 272-276.

[19] K. Yang, J. Liu, R. Si, X. Chen, W. Dai, X. Fu, Comparative study of Au/TiO2 and Au/Al2O3 for oxidizing CO in the presence of H-2 under visible light irradiation, Journal of Catalysis, 317 (2014) 229-239.

[20] T. Shodiya, O. Schmidt, W. Peng, N. Hotz, Novel nano-scale Au/α-Fe2O3 catalyst for the preferential oxidation of CO in biofuel reformate gas, Journal of Catalysis, 300 (2013) 63-69.

[21] L.-H. Chang, N. Sasirekha, Y.-W. Chen, W.-J. Wang, Preferential oxidation of CO in H-2 stream over Au/MnO2-CeO2 catalysts, Industrial & Engineering Chemistry Research, 45 (2006) 4927-4935.

[22] Y.-W. Chen, H.-J. Chen, D.-S. Lee, Au/Co3O4-TiO2 catalysts for preferential oxidation of CO in H-2 stream, Journal of Molecular Catalysis a-Chemical, 363 (2012) 470-480.

[23] T. Tabakova, G. Avgouropoulos, J. Papavasiliou, M. Manzoli, F. Boccuzzi, K. Tenchev, F. Vindigni, T. Ioannides, CO-free hydrogen production over Au/CeO2–Fe2O3 catalysts: Part 1. Impact of the support composition on the performance for the preferential CO oxidation reaction, Applied Catalysis B: Environmental, 101 (2011) 256-265.

[24] M. Cargnello, C. Gentilini, T. Montini, E. Fonda, S. Mehraeen, M. Chi, M. Herrera-Collado, N.D. Browning, S. Polizzi, L. Pasquato, P. Fornasiero, Active and Stable Embedded Au@CeO2 Catalysts for Preferential Oxidation of CO, Chemistry of Materials, 22 (2010) 4335-4345.

[25] T. Tabakova, G. Avgouropoulos, J. Papavasiliou, M. Manzoli, F. Boccuzzi, K. Tenchev, F. Vindigni, T. Ioannides, CO-free hydrogen production over Au/CeO2-Fe2O3 catalysts: Part 1. Impact of the support composition on the performance for the preferential CO oxidation reaction, Applied Catalysis B-Environmental, 101 (2011) 256-265.

[26] J. Fonseca, S. Royer, N. Bion, L. Pirault-Roy, M.d.C. Rangel, D. Duprez, F. Epron, Preferential CO oxidation over nanosized gold catalysts supported on ceria and amorphous ceria-alumina, Applied Catalysis B-Environmental, 128 (2012) 10-20.

[27] E. de Oliveira Jardim, S. Rico-Frances, F. Coloma, E.V. Ramos-Fernandez, J. Silvestre-Albero, A. Sepulveda-Escribano, Superior performance of gold supported on doped CeO2 catalysts for the preferential CO oxidation (PROX), Applied Catalysis a-General, 487 (2014) 119-129.

[28] W.S. Shin, C.R. Jung, J. Han, S.W. Nam, T.H. Lim, S.A. Hong, H.I. Lee, Development of Au/CeO2 catalysts for preferential oxidation of CO in PEMFC, Journal of Industrial and Engineering Chemistry, 10 (2004) 302-308.

[29] Y. Duan, M. Xu, X. Zhou, X. Huai, A structured packed-bed reactor designed for exothermic hydrogenation of acetone, Particuology, 17 (2014) 125-130.

[30] M. Ruta, I. Yuranov, P.J. Dyson, G. Laurenczy, L. Kiwi-Minsker, Structured fiber supports for ionic liquid-phase catalysis used in gas-phase continuous hydrogenation, Journal of Catalysis, 247 (2007) 269-276.

[31] P. Frontera, L.A. Scarpino, C. Busacca, P.L. Antonucci, S. Siracusano, A.S. Aricò, High surface area Ti-based mixed oxides nanofibers prepared by electrospinning, Materials Letters, 134 (2014) 281-285.

[32] J.J. Schneider, M. Naumann, C. Schaefer, A. Brandner, H.J. Hofmann, P. Claus, Template-assisted formation of microsized nanocrystalline CeO2 tubes and their catalytic performance in the carboxylation of methanol, Beilstein Journal of Nanotechnology, 2 (2011) 776-784.

[33] J.L. Hueso, V. Sebastian, A. Mayoral, L. Uson, M. Arruebo, J. Santamaria, Beyond gold: rediscovering tetrakis-(hydroxymethyl)-phosphonium chloride (THPC) as an effective agent for the synthesis of ultra-small noble metal nanoparticles and Pt-containing nanoalloys, Rsc Advances, 3 (2013) 10427-10433.

[34] J.S. Yun, C.K. Park, J.H. Cho, J.-H. Paik, Y.H. Jeong, J.-H. Nam, K.-R. Hwang, The effect of PVP contents on the fiber morphology and piezoelectric characteristics of PZT nanofibers prepared by electrospinning, Materials Letters, 137 (2014) 178-181.

[35] S.H. Tan, R. Inai, M. Kotaki, S. Ramakrishna, Systematic parameter study for ultra-fine fiber fabrication via electrospinning process, Polymer, 46 (2005) 6128-6134.

[36] C. Mit-uppatham, M. Nithitanakul, P. Supaphol, Ultrafine electrospun polyamide-6 fibers: Effect of solution conditions on morphology and average fiber diameter, Macromolecular Chemistry and Physics, 205 (2004) 2327-2338.

[37] Y. Xin, Z. Huang, J. Chen, C. Wang, Y. Tong, S. Liu, Fabrication of well-aligned PPV/PVP nanofibers by electrospinning, Materials Letters, 62 (2008) 991-993.

[38] F. Li, X. Yu, H. Pan, M. Wang, X. Xin, Syntheses of MO2 (M=Si, Ce, Sn) nanoparticles by solid-state reactions at ambient temperature, Solid State Sciences, 2 (2000) 767-772.

[39] X. Li, F. Chen, X. Lu, C. Ni, Z. Chen, Modified-EISA synthesis of mesoporous high surface area CeO2 and catalytic property for CO oxidation, Journal of Rare Earths, 27 (2009) 943-947.

[40] P. Sudarsanam, B. Mallesham, D.N. Durgasri, B.M. Reddy, Physicochemical and catalytic properties of nanosized Au/CeO2 catalysts for eco-friendly oxidation of benzyl alcohol, Journal of Industrial and Engineering Chemistry, 20 (2014) 3115-3121.

[41] E.d.O. Jardim, S. Rico-Francés, F. Coloma, E.V. Ramos-Fernández, J. Silvestre-Albero, A. Sepúlveda-Escribano, Superior performance of gold supported on doped CeO2 catalysts for the preferential CO oxidation (PROX), Applied Catalysis A: General, 487 (2014) 119-129.

[42] M. Škoda, M. Cabala, I. Matolínová, K.C. Prince, T. Skála, F. Šutara, K. Veltruská, V. Matolín, Interaction of Au with CeO2(111): A photoemission study, The Journal of Chemical Physics, 130 (2009) -.

[43] N. Ta, J. Liu, S. Chenna, P.A. Crozier, Y. Li, A. Chen, W. Shen, Stabilized Gold Nanoparticles on Ceria Nanorods by Strong Interfacial Anchoring, Journal of the American Chemical Society, 134 (2012) 20585-20588.

[44] K. Tsutsumi, H. Yoshitake, Coupling reaction between α,β-unsaturated aldehyde and methanol catalysed by gold-supported on mesostructured cerias, Applied Catalysis A: General, 484 (2014) 64-73.

[45] S.M.F. Shahed, T. Hasegawa, Y. Sainoo, Y. Watanabe, N. Isomura, A. Beniya, H. Hirata, T. Komeda, STM and XPS study of CeO2(111) reduction by atomic hydrogen, Surface Science, 628 (2014) 30-35.

[46] P. Sudarsanam, B. Mallesham, P.S. Reddy, D. Großmann, W. Grünert, B.M. Reddy, Nano-Au/CeO2 catalysts for CO oxidation: Influence of dopants (Fe, La and Zr) on the physicochemical properties and catalytic activity, Applied Catalysis B: Environmental, 144 (2014) 900-908.

[47] L. Delannoy, N. Weiher, N. Tsapatsaris, A.M. Beesley, L. Nchari, S.L.M. Schroeder, C. Louis, Reducibility of supported gold (III) precursors: influence of the metal oxide support and consequences for CO oxidation activity, Topics in Catalysis, 44 (2007) 263-273.

[48] Y. Zhou, E.W. Peterson, J. Zhou, Effect of nature of ceria supports on the growth and sintering behavior of Au nanoparticles, Catalysis Today, 240, Part B (2015) 201-205.

[49] S.T. Oyama, X. Zhang, J. Lu, Y. Gu, T. Fujitani, Epoxidation of propylene with H2 and O2 in the explosive regime in a packed-bed catalytic membrane reactor, Journal of Catalysis, 257 (2008) 1-4.

[50] D.I. Potemkin, E.Y. Semitut, Y.V. Shubin, P.E. Plyusnin, P.V. Snytnikov, E.V. Makotchenko, D.Y. Osadchii, D.A. Svintsitskiy, S.A. Venyaminov, S.V. Korenev, V.A. Sobyanin, Silica, alumina and ceria supported Au–Cu nanoparticles prepared via the decomposition of [Au(en)2]2[Cu(C2O4)2]3·8H2O single-source precursor: Synthesis, characterization and catalytic performance in CO PROX, Catalysis Today, 235 (2014) 103-111.

[51] L. Qi, C. Tang, L. Zhang, X. Yao, Y. Cao, L. Liu, F. Gao, L. Dong, Y. Chen, Influence of cerium modification methods on catalytic performance of Au/mordenite catalysts in CO oxidation, Applied Catalysis B: Environmental, 127 (2012) 234-245.

[52] J.A. Rodriguez, R. Si, J. Evans, W. Xu, J.C. Hanson, J. Tao, Y. Zhu, Active gold-ceria and gold-ceria/titania catalysts for CO oxidation: From single-crystal model catalysts to powder catalysts, Catalysis Today, 240, Part B (2015) 229-235.

[53] S.E. Collins, J.M. Cies, E. del Rio, M. Lopez-Haro, S. Trasobares, J.J. Calvino, J.M. Pintado, S. Bernal, Hydrogen interaction with a ceria-zirconia supported gold catalyst. Influence of CO co-adsorption and pretreatment conditions, Journal of Physical Chemistry C, 111 (2007) 14371-14379.

[54] S. Scirè, C. Crisafulli, P.M. Riccobene, G. Patanè, A. Pistone, Selective oxidation of CO in H2-rich stream over Au/CeO2 and Cu/CeO2 catalysts: An insight on the effect of preparation method and catalyst pretreatment, Applied Catalysis A: General, 417–418 (2012) 66-75.

[55] J. Fonseca, S. Royer, N. Bion, L. Pirault-Roy, M.d.C. Rangel, D. Duprez, F. Epron, Preferential CO oxidation over nanosized gold catalysts supported on ceria and amorphous ceria–alumina, Applied Catalysis B: Environmental, 128 (2012) 10-20.

[56] T. Sakwarathorn, A. Luengnaruemitchai, S. Pongstabodee, Preferential CO oxidation in H2-rich stream over Au/CeO2 catalysts prepared via modified deposition–precipitation, Journal of Industrial and Engineering Chemistry, 17 (2011) 747-754.

[57] L.F. Liotta, G. Di Carlo, G. Pantaleo, A.M. Venezia, Supported gold catalysts for CO oxidation and preferential oxidation of CO in H2 stream: Support effect, Catalysis Today, 158 (2010) 56-62.